remote sensing

MDPI

Article

Spatial Scale Effect and Correction of Forest Aboveground Biomass Estimation Using Remote Sensing

Ying Yu [1,2], Yan Pan [1,2], Xiguang Yang [1,2,*] and Wenyi Fan [1,2]

[1] School of Forestry, Northeast Forestry University, Harbin 150040, China; yuying@nefu.edu.cn (Y.Y.); 2020121174@nefu.edu.cn (Y.P.); fanwy@nefu.edu.cn (W.F.)
[2] Key Laboratory of Sustainable Forest Ecosystem Management, Ministry of Education, Northeast Forestry University, Harbin 150040, China
* Correspondence: yangxiguang@nefu.edu.cn

Abstract: Forest biomass is critically important for forest dynamics in the carbon cycle. However, large-scale AGB mapping applications from remote sensing data still carry large uncertainty. In this study, an AGB estimation model was first established with three different remote sensing datasets of GF-2, Sentinel-2 and Landsat-8. Next, the optimal scale estimation result was considered as a reference AGB to obtain the relative true AGB distribution at different scales based on the law of conservation of mass, and the error of the scale effect of AGB estimation at various spatial resolutions was analyzed. Then, the information entropy of land use type was calculated to identify the heterogeneity of pixels. Finally, a scale conversion method for the entropy-weighted index was developed to correct the scale error of the estimated AGB results from coarse-resolution remote sensing images. The results showed that the random forest model had better prediction accuracy for GF-2 (4 m), Sentinel-2 (10 m) and Landsat-8 (30 m) AGB mapping. The determination coefficient between predicted and measured AGB was 0.5711, 0.4819 and 0.4321, respectively. Compared to uncorrected AGB, R^2 between scale-corrected results and relative true AGB increased from 0.6226 to 0.6725 for Sentinel-2, and increased from 0.5910 to 0.6704 for Landsat-8. The scale error was effectively corrected. This study can provide a reference for forest AGB estimation and scale error reduction for AGB production upscaling with consideration of the spatial heterogeneity of the forest surface.

Keywords: forest aboveground biomass (AGB); scale effect; random forest (RF); scale correction

Citation: Yu, Y.; Pan, Y.; Yang, X.; Fan, W. Spatial Scale Effect and Correction of Forest Aboveground Biomass Estimation Using Remote Sensing. *Remote Sens.* **2022**, *14*, 2828. https://doi.org/10.3390/rs14122828

Academic Editor: Klaus Scipal

Received: 28 April 2022
Accepted: 10 June 2022
Published: 13 June 2022

1. Introduction

Terrestrial ecosystems, covering approximately 30% of the Earth's land surface, play an important role in the global carbon cycle and climate changes [1]. Forests are a major contributor to the terrestrial carbon pool. Forests store approximately 45% of the carbon found in terrestrial ecosystems as living biomass and dead wood and litter [2,3]. At the same time, forests can sequester large amounts of carbon dioxide from the atmosphere and contribute approximately 50% of the global net primary production (NPP) and approximately 80% of terrestrial NPP [4–6]. Forests absorb atmospheric CO_2 through photosynthesis and remove nearly 3 billion tons of anthropogenic carbon every year [7]. As forests grow, around 30% of CO_2 emissions from fuel burning and net deforestation are absorbed [8]. Therefore, forest ecosystems can increase or decrease carbon sequestration by restoring or degrading vegetation [9]. If a forest is disturbed by fire, deforestation or other human factors, the carbon stored in the forest would be released back into the atmosphere; therefore, the accurate estimation of forest carbon stocks is essential for the study of the carbon exchange between terrestrial ecosystems and the atmosphere and its effects on ecosystem-level carbon cycling, feeding back to climate change [10,11].

Forest aboveground biomass, or aboveground biomass of trees (AGB), is defined as the mass of the living organic material, which includes the living stems, branches and leaves of vegetation, with units of mass per unit area [12]. The aboveground biomass constitutes the main portion of the carbon stock, and it is the most important and visible terrestrial ecosystem carbon pool. The AGB is intimately related to the emission of CO_2 caused by land use change and fire and the stored CO_2 in the atmosphere by vegetation growth. AGB is a key quantity estimating terrestrial carbon pools and is recognized as an Essential Climate Variable (ECV) by the Global Climate Observing System (GCOS) [13]. It is also used to monitor climate change by the United Nations Framework Convention on Climate Change (UNFCCC) and the Intergovernmental Panel on Climate Change (IPCC) [14]. In addition, vegetation biomass has also wider significance to human society in the form of food, materials, energy and other ecosystem services that can be found in forests and other ecosystems [15]. AGB is also important for monitoring the forest planting dynamics, evaluating forest management practices and assessing wood resources [15,16]. Accurately monitoring and reporting the forest aboveground biomass is essential to correctly budget carbon emissions and is beneficial for mitigating climate change through the reduction of greenhouse gas emissions [17].

Conventionally, the AGB estimation methods can be categorized into field measurement, ecological model simulation and approaches involving remote sensing [1]. Field measurement requires an intensive field inventory; the most important field forest-related parameters include the number of trees, tree density, the taxonomical information, tree height and the diameter at breast height (DBH) [18]. Field measurement is considered to provide the most accurate AGB estimation, combined with allometric equations [19]. The traditional approach of manual data collection is called field inventory in forestry [20]. It is an important method that is used in the monitoring and management of the forest. However, the conventional method of AGB inventory is destructive, labor-intensive, expensive, time-consuming and sometimes limited by poor accessibility [21]. It cannot provide the spatial and temporal distribution and explicit forest biomass information [1]. Hence, the field inventory method is practical only in relatively smaller areas [22].

Limited by the traditional methods of AGB estimation on a regional scale, remote sensing has been widely used to estimate AGB during the past few decades. On the one hand, remote sensing technology has the advantage of facilitating the collection of forest type characteristics and coverage information, which is greatly useful in field inventory [23]. On the other hand, remote sensing can provide the spectral characteristics of vegetation and offer the repeated historical observation required for change detection, and digital data can be easily stored and integrated with geographic information [22]. Remote sensing technology has been extensively used as an efficient and economical method for the large-scale estimation of forest biomass [24,25]. Various remote sensing data, such as optical, thermal, microwave, radar and LiDAR remote sensing data, have been used for AGB estimation [26,27]. The intermediate- and high-resolution remote sensing are usually used for biomass estimation at local or sub-regional scales, such as Landsat series, SPOT, WorldView-2 and GF series [28–30]. Moreover, MODIS and NOAA-AVHRR remote sensing data have been used to estimate AGB at a regional, national or global scale [31,32]. Optical remote sensing data are a common data source for biomass estimation, but data saturation in the optical regime is an important factor influencing the accuracy of biomass estimation in forests [33,34]. With the rapid development of light detection and ranging (LiDAR) technology, LiDAR has become a vital method for AGB estimation [35]. Compared to optical remote sensing, LiDAR can derive the canopy height information, which is strongly related to AGB at high levels, and it is considered the most promising technique for biomass estimation. However, LiDAR data are usually limited to use in small areas due to high costs [26].

In the last few decades, multiple-resource remote sensing data have been used to estimate AGB and are recognized as dominant data sources for AGB mapping [1]. However, current AGB estimations were retrieved by using different methods and remote sensing data with various spatial resolutions [36]. This would lead to significant disagreement when estimating AGB and reduce its value in global and national applications. There are many random and/or systematic errors that arise during AGB estimation, such as in field-based AGB estimation, matching field and remote sensing measurement, satellite-based measurement and global wall-to-wall extrapolation [37]. First, the uncertainty of the field-based AGB estimation is a matter of concern for remote sensing scholars. Chen et al. tracked the errors from the field-based uncertainty of AGB estimation based on airborne LiDAR remote sensing [38]. Longo et al. concluded that the field-based uncertainty contributed around 10% of the total pixel-level uncertainty of AGB prediction at a 0.16 ha resolution [39]. Second, the mismatch between field measurements and remote sensing images may lead to errors in AGB estimation. Moreover, it would reduce the AGB model error from 51% to 4% at 20 to 100 m resolution when using LiDAR remote sensing [40]. The spatial difference between field measurements and remote sensing data is a common problem that can increase the AGB estimation error in remote sensing studies [41]. Næsset et al. found that the field plot size would have an effect on the estimation of AGB and pointed out that the plot size should be considered when using remotely sensed data for AGB estimation [42]. Persson et al. analyzed the uncertainties of AGB estimation at the plot and stand level and concluded that the error of field-based AGB estimation cannot be ignored, such as measured errors, missed or double-counted trees, measurement errors, sample plot location positioning errors or erroneous registration of tree species [43]. Moreover, this uncertainty is difficult to predict in natural forests, but the error can be reduced with an increase in the plot size [44]. In addition, Shen pointed out that the distribution of survey sites may bring some uncertainty in AGB estimation [45]. Lastly, the issue of the scale mismatch between the calibration of the field measurement and remote sensing pixels is a significant challenge. When coarse-resolution remote sensing is used to map the local- or national-scale AGB, the numerous data of small field plots, such as national forest inventory datasets, will be used to establish the AGB estimation model. However, the area of the most of the field plots is less than 0.1 ha in size. Réjou-Méchain et al. analyzed the local spatial variability of AGB in plots with the size of 0.1 ha and 100 ha. Results show that the local spatial variability is large for standard plots, and the value of the local spatial variability is 46.3% for 0.1 ha subplots and 16.6% for 1 ha subplots, respectively [46]. Compared with large plots, small plots carry large errors due to AGB variability for a consistent pixel-to-plot size. Moreover, this will generate large sampling errors and produce significant bias when estimating an AGB map. Thus, field measurements that better match the remote sensing pixel resolution are a challenge, and a more reliable approach to minimizing this sampling error needs to be developed.

It is complex to assess and quantify of the AGB estimation errors by using remote sensing data. However, it is also important to identify the errors and assess the effect of the different spatial resolutions of remote sensing data on AGB estimation, as it contributes to the uncertainty of the RS-based estimation; it is also necessary to consider how to correct this error. In this study, the issue of the scale mismatch of AGB estimation for remote sensing of different spatial resolutions was discussed. Moreover, a novel method, which is based on the law of conservation of mass, was developed, and the errors of the scale effect of AGB estimation at various spatial resolutions were analyzed. To achieve this goal, an AGB estimation model was first established that referred to three different spatial resolutions of remote sensing data, and the accuracy of AGB estimation at three different scales was analyzed. Second, the optimal scale estimation result was considered as a reference AGB spatial distribution true value, and the mismatch error due to the spatial variability and non-linearity of the AGB estimation model was discussed at three different spatial resolutions of remote sensing. Third, the scale conversion method of the entropy-weighted index with the assumption of the average AGB constant in this region, which was used to correct the scale error of AGB estimation by using coarse-resolution remote sensing, was established and the weight coefficient was determined by analyzing the biases between estimated and true AGB values. Finally, the AGB map with coarse-resolution remote sensing was corrected. This research represents an approach to the scale error correction of AGB estimation by using coarse-resolution remote sensing, and it provides a reference for high-precision AGB mapping using coarse-resolution remote sensing at a regional, national or global scale.

2. Study Area and Data

2.1. Study Area

The study area is located at the Maoer Mountain Experimental Forest Farm (127°29′–127°44′E, 45°14′–45°29′N), Shangzhi City, Heilongjiang Province, Northeast China (Figure 1). The area of the Maoer Mountain Forest Farm is approximately 26.496 km^2. Maoer Mountain belongs to the offset of the Changbai Mountains and extends to the northwest offset of the Zhangguangcai Range. The study area is a low mountainous and hilly area. The terrain of the forest area gradually rises from south to north, with an average altitude of 300 m. The research region belongs to the mid-temperate continental monsoon climate zone. The annual average temperature is around 2.7 °C, and the annual precipitation is around 649 mm. The average temperature of the hottest month of July is 21.8 °C, and January is the coldest month, with average temperatures of −19.9 °C [47]. The average annual thermal amplitude is 41.7 °C. The average forest coverage rate is 95%, and the total forest volume is 3.5 million m^3. The main tree species are Korean pine (*Pinus koraiensis*) mixed with deciduous species including birch (*Betula* spp.), larch (*Larix* spp.), poplar (*Populus* spp.), sylvestris pine (*Pinus sylvestris*) and Mongolian oak (*Quercus* spp.) [47,48].

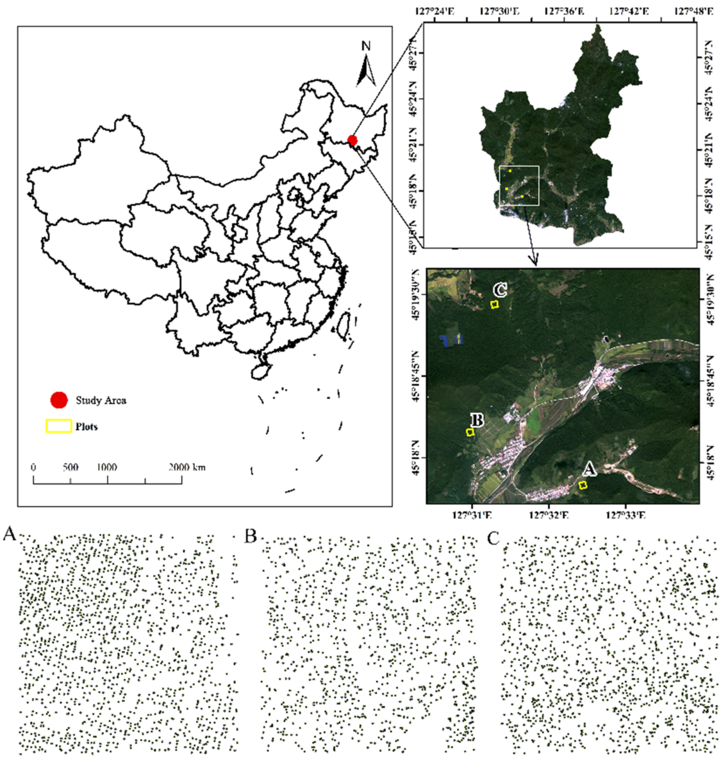

Figure 1. Study area and sample site location. (**A**) the distribution of single trees in the plot of the broadleaf forest; (**B**) the distribution of single trees in the plot of coniferous forest; (**C**) the distribution of single trees in the plot of the coniferous and broadleaf mixed forest.

2.2. Data

2.2.1. Remote Sensing Data and Pre-Processing

Three different spatial resolutions of remote sensing data, including GF-2, Sentinel-2 and Landsat-8 OLI, were used in this study.

Gaofen-2 (GF-2) is a civilian optical remote sensing satellite. The GF-2 satellite was launched by the China National Space Administration (CNSA) on 19 August 2014. GF-2 is the first satellite in China with a resolution below 1 m and captures high-resolution remote sensing images. It has been widely used in land use investigation, monitoring of the environmental atmosphere and water environment, urban planning, monitoring of disasters and resource surveys [49]. The GF-2 satellite platform is equipped with a panchromatic band with a 1 m spatial resolution and four multispectral band scanners with 4 m resolution, spatial including red (R), green (G), blue (B) and near-infrared (NIR). GF-2 can achieve a swath width of 45 km ground observation at one time and the revisiting time of GF-2 is 69 days. The remote sensing data were collected in August 2019.

The pre-processing of the GF-2 remote sensing images included the following: (1) radiation calibration for spectral channels was multiplied by gain and bias coefficients; (2) atmospheric correction was carried out by using the fast line-of-sight atmospheric analysis of the spectral hypercubes (FLAASH) model to obtain the surface reflectance; (3) geometric correction was performed. The GF-2 images were corrected based on a 1:10,000 topographic map with the method of polynomial and bilinear interpolation resampling. Then, the vegetation indices used in this study were calculated.

Sentinel-2A and 2B were designed by the European Space Agency (EAS) to meet the needs of the Copernicus program. The Sentinel-2A satellite was launched on 23 June 2015, followed by Sentinel-2B on 7 March 2017. The Sentinel-2A satellite has 13 bands covering the visible to shortwave infrared (SWIR) wavelength regions and it collects multispectral remote sensing data. The swath width of Sentinel-2A is 290 km and the revisiting time is 10 days. The spatial resolutions of Sentinel-2A data included four bands from visible and near-infrared (NIR) with a spatial resolution of 10 m, six bands from red-edge to shortwave infrared (SWIR) with a spatial resolution of 20 m and three atmospheric correction bands with a spatial resolution of 60 m, respectively [50]. Sentinel-2A Level-1C production with 10 m resolution was used in this study. The Sentinel-2A Level-1C data were obtained at the end of July 2019.

The pre-processing of the Sentinel-2A remote sensing images included the following: (1) resampling, in which all the bands were resampled to 10 m resolution; (2) atmospheric correction and terrain correction, which was carried out using the ESA SEN2COR processor to obtain the surface reflectance. Then, the vegetation indices used in this study were calculated.

The Landsat-8 Operational Land Imager (OLI) is an instrument in the Landsat series of satellite imagers. It was launched in February 2013. The Landsat-8 OLI continues the legacy of the Landsat series and adds two bands of the cirrus clouds and a coastal/aerosol (CA) band to detect water and aerosols in the blue region with a better resolution [51]. Landsat-8 OLI images consist of 11 spectra with a spatial resolution of 30 m. The images of Landsat-8 OLI data were acquired in July 2019.

The pre-processing of the Landsat-8 OLI remote sensing images included radiometric calibration, atmospheric correction, terrain correction and geometric correction. All the pre-processing of satellite data was conducted using ENVI 5.3 software (developed by Exelis Visual Information Solutions, Inc., Boulder, CO, USA).

2.2.2. Field Measurement

The ground data survey began in August 2019, and a total of 3 rectangular plots with a size of 100 m $\times$ 100 m were laid out (see Figure 1). The forest type of the sample plots included coniferous forests, broad-leaved forests and mixed forest types. The plot of the coniferous forest was mainly composed of Korean pine and larch, and the plot of the broad-leaved forest was mainly made up of birch and linden. Before the sample plot investigation, the GPS coordinates of the four corners and the central position of each sample plot were recorded by using a high-precision Differential Global Positioning System (DGPS; produced by Trimble Navigation Limited, Sunnyvale, CA, USA). Then, all trees were numbered and geolocated within each plot. The following forest parameters were then measured: diameter at breast height (DBH), tree height, under branch height, crown width, tree species. All of the trees with diameters at breast height greater than 5 cm in the sample plot were measured.

Stand aboveground biomass was calculated on the basis of established individual tree biomass models. A single-tree univariate additive biomass model established by Dong was used to estimate the single-tree aboveground biomass [52]. First, the biomass of the tree components of the tree stem, branch and leaf was calculated, and the total aboveground biomass of the single tree was the sum of the biomass of the tree components. It is important to note that the root biomass was not included in this study. Then, plot biomass could be derived from the sum of the all living trees' biomass in each sample plot. Finally, the stand aboveground biomass per ground area could be calculated.

For the comparison of the biomass remote sensing estimate at different scales, the large rectangular plot was divided into differently sized subplots. According to the spatial resolution of GF-2, Sentinel-2 and Landsat-8, we divided the 100 m × 100 m plot into several subplots with the size of 4 m ×4 m (GF-2), 10 m × 10 m (Sentinel-2) and 30 m × 30 m (Landsat-8), respectively. Some of the data were selected randomly to establish the AGB prediction model. The AGB statistical information of the selected subset with different sizes is shown in Table 1.

Table 1. The AGB statistical information of the field measurements at pixel scale (Unit: t/ha).

Index	GF-2 (n = 70)	Sentinel-2 (n = 70)	Landsat-8 (n = 55)
Mean	112.7623	98.4261	105.2296
Standard deviation	23.1844	31.0125	31.8978
Range	47.2768–181.5890	47.1336–174.2340	47.9736–193.5593

3. Methodology

3.1. Method of Aboveground Forest Biomass Estimation at Different Spatial Scales

3.1.1. Remote Sensing Variable Selection

The purpose of the AGB modeling was to construct the relationships between the variables extracted from remote sensing data and AGB. The first important step was selecting the variables for AGB estimation. To increase the number of candidates in the independent variable dataset, the spectral indices, vegetation indices, texture features, terrain factors and other parameters of the images of three different spatial resolutions from GF-2, Sentinel-2 and Landsat-8 were extracted as candidate characteristic variables [50,53]. There were a total 62 candidate remote sensing variables extracted from GF-2 satellite data, 57 candidate remote sensing variables extracted from Sentinel-2 satellite data and 63 candidate remote sensing variables extracted from Landsat-8 satellite data.

The significant relationships between the variables of the remote sensing data and AGB demonstrated the candidates for optical remote sensing data for AGB estimation and determined the accuracy of AGB estimation. Therefore, it was very important to screen variables from the remote sensing data carefully for AGB modeling [54]. For the first step, the Pearson correlation coefficient between candidate remote sensing variables and AGB field measurement was calculated, and those variables with a lower correlation coefficient ($R < 0.05$) were removed to improve the quality of the candidate remote sensing variables.

The variable importance in projection (VIP) score is often used to assess the importance of variables. In general, those variables with a greater VIP score are considered to be more important than those with smaller ones [55]. Therefore, we used the VIP score to evaluate the importance of the candidate remote sensing variables in the AGB modeling in the next step. The remaining variables screened in the first step were ranked according to the VIP, calculated with random forest, to screen the independent variables for a second time. Finally, three groups of remote sensing variables were successfully selected to prepare for AGB modeling at three different spatial resolutions of remote sensing. There were 8 remote sensing variables in each group, and the details can be found in Table 2.

Table 2. Selected variables for AGB modeling.

Sensor	Variable	Formular	Description
GF-2	ME2	$\sum_{i,j=0}^{N-1} iP_{ij}$	Mean of the four directional textural features of GF-2 band 2
	Var4	$\sum_{i,j=0}^{N-1} P_{ij}(i-ME)^2$	Sum variance of the gray-level co-occurrence matrix of GF-2 band 4
	Ho2	$\sum_{i,j=0}^{N-1} i\frac{P_{ij}}{1+(i-j)^2}$	Homogeneity of the gray-level co-occurrence matrix of GF-2 band 2
	B1	Blue, 450–520 nm	Reflectance of the GF-2 blue band
	B431 [56]	(B4 + B3)/B1	A vegetation index calculated by GF-2 band 1, 3 and 4
	B4	Near-infrared band, 770–890 nm	Reflectance of the GF-2 near-infrared band
	B13	B1 + B3 [56]	A vegetation index calculated by GF-2 band 1 and 3
	PX	Slope	Slope extracted from DEM data resampled to GF-2 spatial resolution
Sentinel-2	Var7	$\sum_{i,j=0}^{N-1} P_{ij}(i-ME)^2$	Sum variance of gray-level co-occurrence matrix of Sentinel-2 band 7
	Cor8	$\sum_{i,j=0}^{N-1} iP_{ij}\left[\frac{(i-ME)(j-ME)}{\sqrt{VA_iVA_j}}\right]$	The correlation texture between the grey levels and those neighboring pixels of Sentinel-2 band 8
	IRECI [57]	(B7 − B4)/(B5/B6)	Inverted red-edge chlorophyll index
	B3	Green, 560 nm	Reflectance of the Sentinel-2 green light band
	PX	Slope	Slope extracted from DEM data resampled to Sentinel-2 spatial resolution
	Wetness [58]	0.2578 × B2 + 0.2305 × B3 + 0.0883 × B4 + 0.1071 × B8 − 0.7611 × B11 − 0.5308 × B12 [59]	Tasseled Cap (KT) transformation wetness
	REIP [57]	700 + 40 × [(B4 + B7)/2 − B5]/(B6 − B5)	Red-edge infection point index
	Brightness [58]	0.351 × B2 + 0.3813 × B3 + 0.3437 × B4 + 0.7196 × B8 + 0.2396 × B11 + 0.1949 × B12 [59]	Tasseled Cap (KT) transformation brightness
Landsat-8	B4/Albedo [60]	B4/(0.246 × B2 + 0.146 × B3 + 0.191 × B4 + 0.304 × B5 + 0.105 × B6 + 0.008 × B7)	Band combination vegetation index
	PX	Slope	Slope extracted from DEM data resampled to Landsat-8 spatial resolution
	B4	Red, 640–670 nm	Reflectance of the Landsat-8 red light band
	ND563 [60]	(B5 + B6 − B3) × (B5 + B6 + B3)	Normalized difference vegetation index

Table 2. *Cont.*

Landsat-8	Cor5	$\sum_{i,j=0}^{N-1} iP_{ij}\left[\frac{(i-ME)(j-ME)}{\sqrt{VA_i VA_j}}\right]$	The correlation texture between the grey levels and those neighboring pixels of Landsat-8 band 5
	SM5	$\sum_{i,j=0}^{N-1} P_{i,j}$	Angular second moment of Landsat-8 band 5
	Var5	$\sum_{i,j=0}^{N-1} P_{ij}(i-ME)^2$	Sum variance of gray-level co-occurrence matrix of Landsat-8 band 5
	ME2	$\sum_{i,j=0}^{N-1} iP_{ij}$	Mean of the four directional textural features of Landsat-8 band 2

(Note: The variables of the P (i, j) refer to the value at the position of (i,j) in a gray-level co-occurrence matrix, where i and j are the number of the rows and columns in the gray-level co-occurrence matrix. The variable of N is the number of rows or columns of the gray-level co-occurrence matrix. ME and VA are the mean and variance of the four directional textural features, respectively).

3.1.2. Method of AGB Modeling

In this study, a random forest (RF) algorithm was conducted to estimate the AGB of the research area. Then, multiple linear regression (MLR) was used to compare the accuracy of AGB estimation.

Random forest (RF) is a machine learning algorithm proposed by Leo Breiman (2001) [61]. Random forest was developed based on multiple regression trees; it shows that the relationship between an input relates to its dependent variable by using multiple regression trees [62]. The main advantage of RF is the ability to describe complex nonlinear relationships, such as in a complex ecological system. It is more effective than a linear regression model for multi-variable models. Thus, a random forest algorithm was selected to effectively predict forest AGB by using remote sensing data. Moreover, the number of regression trees was set to 1000 and the random state of the random forest algorithm was set to 10 in this study.

A traditional multiple linear regression (MLR) was applied as a baseline for AGB model accuracy comparison. A backward stepwise multiple linear regression was performed to establish the forest AGB retrieval model. The formula of the MLR is as follows:

$$y = \beta 0 + \beta 1 \times 1 + \beta 2 \times 2 + \ldots + \beta n \times n + \varepsilon \tag{1}$$

where y is the variable of the forest AGB; xi is a dataset of remote sensing variables; βi is a fitting parameter; ε is an error term.

Using random sampling, a total of 75% of the sample data were selected for the model establishment, while the remaining 25% of the sample data were employed for the accuracy evaluation.

3.2. Scale Error Calculation

Resampling of the field-measured data or remote sensing AGB production to a consistent spatial resolution with remote sensing data is a commonly used method of error evaluation. Thus, we used two upscaling paths to calculate the AGB from the coarse-resolution remote sensing data and compared the results of these two methods, after which the scale error could be determined (Figure 2).

Figure 2 is a schematic flowchart of the two upscaling methods of AGB estimation. The first method aimed to estimate AGB by using high-resolution remote sensing data and then aggregate the estimated AGB to coarse-resolution remote sensing (Path 1). We named this path "first inversion and then aggregation". The other method was to aggregate the characteristic variables of high-resolution remote sensing images, such as various vegetation indices, to coarse-resolution remote sensing and then estimate the AGB using the remote sensing inversion model of AGB. We named this path "first aggregation and then inversion".

The first path (Path 1) retrieved the AGB through high-resolution remote sensing and resampled the AGB results to coarse-resolution remote sensing by summation. First, we obtained the characteristic variable (V_i) from the high-resolution remote sensing image and established the AGB estimation model ($AGB_i = f_1(V_i)$); then, we inverted the AGB (AGB_i) from the high-resolution remote sensing image (Path 1 step one) and resampled the inverted AGB to coarse-resolution remote sensing by summation (Path 1, Step 2). The calculated AGB with the coarse resolution is the sum of the AGB estimated from high-resolution data. This is often referred to as a distributed algorithm. As a linear transformation, the statistical information of AGB at coarse resolution obtained by this upscaling method was consistent with AGB at the high resolution [63]. Thus, this AGB estimation can be considered as the relative true value of the biomass at the coarse-resolution pixel, defined as AGB_{exa}.

The second path (Path 2) aggregated the characteristic variable of the high-resolution remote sensing to coarse-resolution remote sensing (V_m) first (Path 2, Step 1). This meant that the high-resolution remote sensing should resample to the same spatial resolution with the coarse-resolution remote sensing. Then, an AGB estimation method ($AGB_{app} = f_2(V_m)$)

was established based on the resampled characteristic variable (V_m), and the AGB_{app} could be retrieved from the coarse-resolution remote sensing data (Path 2, Step 2). This is commonly referred to as the lumped algorithm. This process (Path 2, Step 1) can be understood as the imaging process of the coarse-spatial-resolution satellite sensor. The estimated AGB results contained the scale error due to the heterogeneity of the surface feature [64,65]. This can be considered as an estimation of the coarse-resolution pixel biomass, defined as AGB_{app}.

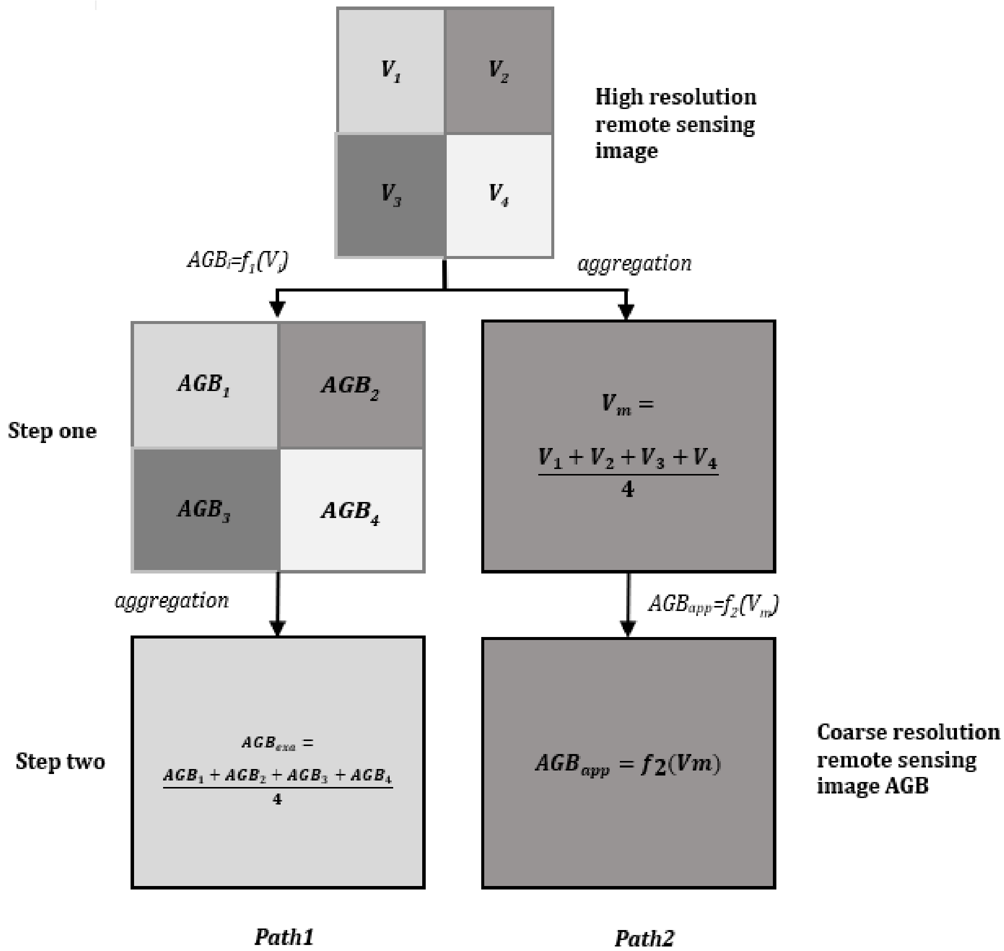

Figure 2. Schematic flowchart of the two upscaling methods of the AGB estimation. (f_i is the remote sensing inversion model of forest aboveground biomass; $V_{(i=1,2,3,4)}$ is the characteristic variable of the high-resolution remote sensing image; V_m is the average value of V_i, namely the pixel V value of the coarse-resolution image; AGB_{exa} is the biological value of the high-resolution image, namely the relative truth value; AGB_{app} is the biological value of the coarse-resolution image, namely the biological values with scale errors).

At present, it is recognized by the academic community that the spatial heterogeneity of surface features is the major reason for the scale effect [66,67]. In other words, it is assumed that multiple spatially heterogeneous, high-resolution pixels are contained in a single coarse-resolution pixel. Due to the heterogeneity of the surface feature, the estimated AGB will contain the error of the scale effect. Therefore, spatial heterogeneity serves as the main contributing factor to the scale error e. It can be calculated as follows:

$$e = AGB_{exa} - AGB_{app} \tag{2}$$

The authenticity test of the remote sensing products involved evaluating the accuracy of the AGB product. The field measurement or AGB estimation result obtained by using high-resolution remote sensing was usually used to verify the precision. Currently, the verification of the AGB remote sensing product at coarse resolution is usually performed according to the relationship between field measurements or generated high-spatial-resolution distribution map of AGB and coarse remote sensing estimated AGB result. To analyze the differences in AGB for various spatial resolutions of remote sensing, the forest biomass map using GF-2 was resampled to 10 m and 30 m resolutions using the distributed algorithm (Path 1). The biomass estimation error of the coarse resolution was calculated, and the scale effect from GF-2 to Sentinel-2 and Landsat-8 was analyzed.

3.3. Scale Error Measurement of Mixed Pixels

3.3.1. Determination of the True Mean Value

According to the law of conservation of mass, we assume that the total quality remains uniform and unchanged in any substance system (isolated system) isolated from the surroundings. A fixed study area or a remote sensing image of the research area also can be considered as an isolated material system. Any changes in the resolution within the region would not alter the total surface area of the research area or the mass of the total forest aboveground biomass. Thus, a hypothesis is proposed that the average of the AGB true value at any scale will remain constant. This true value of the AGB was defined as the mass of the forest aboveground biomass per unit surface area at a certain time and under specific spatial conditions.

To understand this, it can be assumed that the total amount of dry matter in a large region was 8 units of mass, and this value contained no measured or system error. We assumed that the surface area was also 8 units of area. The aboveground biomass (AGB) equated to 1 mass per area; the diagram is shown in Figure 3A.

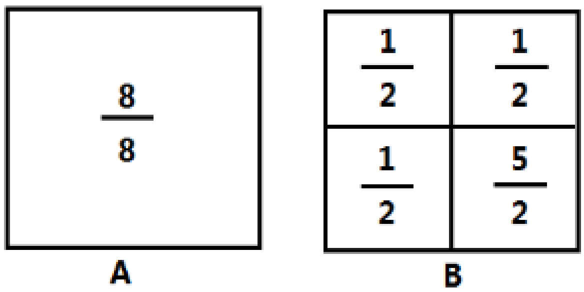

Figure 3. Schematic diagram of true mean AGB scale invariance. (**A**) the mass of the AGB per unit surface area of coarse resolution remote sensing data; (**B**) the mass of the AGB per unit surface area of high resolution remote sensing data.

Then, this large region was divided into 4 equal parts of 2 units of area in each part. The dry matter in each part was assumed as 1, 1, 1 and 5 units of mass due to the spatial heterogeneity. The AGB of each part was 1/2, 1/2, 1/2 and 5/2 mass per area (Figure 3B). However, the average AGB in this region was calculated as [(1/2) + (1/2) +(1/2) + (5/2)]/4 = 1 mass per area. Similarly, if the region was divided into more small units, the average AGB in this region was constant at 1 mass per area under the same condition.

According to the demonstration above, we assumed that the size of the total area was $N \times N$, the size of the remote sensing pixel was $n_j \times n_j$ at j-scale, and the AGB of the ith pixel could be expressed as follows:

$$AGB_{ni} = \frac{1}{n_j^2} \sum_{j=1}^{n_j^2} f\left(V_{j,i}\right) \tag{3}$$

where $f(V_{j,i})$ represented the biomass inversion model of the forest, and $V_{j,i}$ represented the modeled remote sensing variable of the ith pixel at j scale.

Average AGB in this region at the n-scale AGB_n could be expressed as

$$\begin{aligned}
AGB_n &= \frac{1}{\left(\frac{N}{n_j}\right)^2} \sum_{i=1}^{\left(\frac{N}{n_j}\right)^2} AGB_{ni} \\
&= \frac{1}{\left(\frac{N}{n_j}\right)^2} \sum_{i=1}^{\left(\frac{N}{n_j^2}\right)^2} \left[\frac{1}{n_j^2} \sum_{j=1}^{n_j^2} f\left(V_{j,i}\right) \right] \\
&= \frac{1}{\left(\frac{N}{n_j}\right)^2} \frac{1}{n_j^2} \sum_{i=1}^{\left(\frac{N}{n_j}\right)^2} \left[\sum_{j=1}^{n^2} f\left(V_{j,i}\right) \right] \\
= AGB_m &= \frac{1}{\left(\frac{N}{m_j}\right)^2} \sum_{i_m=1}^{\left(\frac{N}{m_j}\right)^2} \left[\frac{1}{n_m^2} \sum_{m=1}^{n_m^2} f_m\left(V_{m,i_m}\right) \right]
\end{aligned} \tag{4}$$

where AGB_m was the average AGB in this region at the m-scale. $f_m(V_{m,i_m})$ represented the biomass inversion model of the forest at m scale and V_{m,i_m} represented the modeled remote sensing variable of the i_mth pixel at m scale.

The various spatial resolutions between remote sensors composed the primary scale effect of the remote sensing image, but the relative true value of AGB at different spatial resolutions was constant, with the average AGB based on measured or other scales in this region. This has been demonstrated previously [68,69]. With the assumption of the average AGB being constant in this region, the high-resolution remote sensing data can be considered as a bridge to connect the field-measured data to the coarse-resolution remote sensing image. Then, the AGB_{exa} retrieved from the high-resolution image was aggregated to a coarse-resolution image pixel AGB_{nexa} (n represented pixel scale). The AGB_{nexa} can be considered as a relative true value of the AGB at the coarse spatial resolution scale. Moreover, compared with the AGB estimation for coarse remote sensing data, the error caused by the scale effect could be evaluated.

3.3.2. Method of Scale Error Correction

According to the scale error formula, the AGB corrected value (AGB_{cor}^{ni}) of each pixel at n-scale can be expressed as an estimated AGB (AGB_{app}^{ni}) of each pixel plus a scale error e_i^n at n-scale, which can be written as:

$$AGB_{cor}^{ni} = AGB_{app}^{ni} + e_i^n \tag{5}$$

e_i^n was the scale error of the ith pixel at n-scale, AGB_{cor}^{ni} was the AGB corrected value of the ith pixel when the pixel scale was n, AGB_{app}^{ni} was the estimated AGB of the ith pixel when the pixel scale was n.

If the estimated AGB (${AGB^n}_{app}$) did not contain a scale error, it should be equal to the relative true AGB at n-scale (${AGB^n}_{exa}$). When the scale error was included in each estimated AGB, the total average error could be considered as the scale effect on AGB estimation. The mean scale error can be calculated as follows:

$$\bar{e}^n = \overline{AGB}_{exa}^n - \overline{AGB}_{app}^n \tag{6}$$

$\bar{e}^n$ referred to the mean scale error of total pixels at n-scale in the research area. $\overline{AGB}_{exa}^n$ was the relative true mean value of the research area AGB, and $\overline{AGB}_{app}^n$ was the mean estimated AGB of the whole research area.

Deduced from the law of large numbers and the central limit theorem, the scale error arithmetic mean e_i^n of samples and its population arithmetic mean $\bar{e}^n$ had the same mathematical expectation and the scale error showed a normal distribution [47]. Then, e_i^n

could be seen as a fluctuation result of the scale error value $\bar{e}^n$ at the point of the pixel i. The range of the fluctuation v_i^n was determined by the difference in the population and sample mean and could be measured by the P_i weight. The fluctuations can be expressed as

$$v_i^n = P_i \times \bar{e}^n \tag{7}$$

Therefore, e_i^n was regarded as the result, which was impacted by the weight P_i of pixel i on the basis of the population value of scale error $\bar{e}^n$. Moreover, e_i^n can be rewritten as:

$$\begin{aligned} e_i^n &= \bar{e}^n + P_i \times \bar{e}^n \\ &= \bar{e}^n \times (1 + P_i) \end{aligned} \tag{8}$$

The coefficient of variation (CV), which was used to measure the relative variation of a random variable to its mean, has been widely used in remote sensing [70]. The coefficient of variation method can be used to evaluate the difference between objects by using the feature of remote sensing. Based on the heterogeneity of the land surface space, the information entropy index was selected to determine the index weight in this study [70]. The formula is as follows [71]:

$$P_i = \sum_{i=0}^{L} -W_i ln W_i \tag{9}$$

where P_i represented the weight of surface heterogeneity calculated by the information entropy from the high-resolution remote sensing data, and W_i was the probability of the occurrence of the i-th land use type. L was the number of land use types included in the high-resolution remote sensing data. According to the information entropy, the weighting index of coarse-resolution pixel-scale space variation was acquired and the scale error could be corrected.

3.3.3. Accuracy Evaluation

After completing the model establishment, four indices were applied for AGB model evaluation, including the determination coefficient (R^2), the root mean squared error (RMSE), the relative root mean squared error (rRMSE) and the mean absolute error (MAE). The equations were as follows [72]:

$$R^2 = 1 - \frac{\sum_{i=1}^{n}(y_i - \hat{y}_i)^2}{\sum_{i=1}^{n}(y_i - \bar{y})^2} \tag{10}$$

$$RMSE = \sqrt{\frac{\sum_{i=1}^{n}(y_i - \hat{y}_i)^2}{n}} \tag{11}$$

$$rRMSE = \sqrt{\frac{\frac{1}{n}\sum_{i=1}^{n}(y_i - \hat{y})^2}{\bar{y}}} \tag{12}$$

$$MAE = \frac{1}{n}\sum_{i=1}^{n}|y_i - \hat{y}_i| \tag{13}$$

where y_i represented the AGB measured value, $\hat{y}$ was the estimated AGB value, $\bar{y}$ referred to the mean value of AGB measured, and n was the number of the samples.

Moreover, another four indices were selected to evaluate the accuracy and efficiency of the upscaling-based method described in this study. These were the mean deviation error (MBE), the root mean squared error (RMSE), average absolute percentage error (MAPE) and determination coefficient (R^2) [73].

$$MBE = \frac{\sum_{i=1}^{n}(p_i - o_i)}{n} \tag{14}$$

$$RMSE = \sqrt{\frac{\sum_{i=1}^{n}(p_i - o_i)^2}{n}} \tag{15}$$

$$MAPE = \frac{100}{n} \times \sum_{i=1}^{n} \frac{|p_i - o_i|}{\overline{p}} \tag{16}$$

$$R^2 = 1 - \frac{\sum_{i=1}^{n}(p_i - o_i)^2}{\sum_{i=1}^{n}(p_i - \overline{o})^2} \tag{17}$$

In the above formula, p_i was the relative true value of AGB at a coarse resolution, $\overline{p}$ was the mean of the p_i, o_i was the estimated AGB after the scale effect correction for a coarse-resolution image, $\overline{o}$ was the mean of the o_i, i was the i-th pixel for a coarse-resolution image, n was the pixel number of a coarse-resolution image.

4. Results

4.1. Results of the AGB Modeling at Various Spatial Resolutions of Remote Sensing

AGB estimation modeling using remote sensing is an important method for large-scale biomass estimation and is a relevant field in remote sensing research [74,75]. Therefore, a large number of extracted vegetation indices, spectral indices and texture variables have been developed for AGB prediction [76–78]. To select the optimal variables, Pearson's correlation coefficient and the VIP score were calculated and eight remote sensing variables were selected; see Table 2. Then, the AGB estimation model was established by using the random forest algorithm and multiple linear regression (MLR) method, and Table 3 shows the performance of the six models using the two modeling methods (Table 3).

Table 3. The comparation of the AGB modeling accuracy with various remote sensing data.

Image	Resolution	Model	R^2	RMSE	MAE	rRMSE
GF-2	4 m	Multiple Linear	0.5110	19.4328	15.7262	0.1737
		Random Forest	**0.5943**	**17.5056**	**14.2677**	**0.1282**
Sentinel-2	10 m	Multiple Linear	0.5409	21.4195	17.7690	0.2442
		Random Forest	0.4971	20.2485	14.9274	0.2308
Landsat-8	30 m	Multiple Linear	0.3034	28.8477	23.7357	0.2778
		Random Forest	0.4235	28.6546	25.2203	0.2759

The modeling accuracy of the random forest model using GF-2 was calculated. The R^2, RMSE, MAE and rRMSE were 0.5943, 17.5056, 14.2677 and 0.1282, respectively. By contrast, the multiple linear regression model established between AGB and the GF-2 feature had lower accuracy (R^2 = 0.5110, RMSE = 19.4328, MAE = 15.7262, rRMSE = 0.1737). For Sentinel-2 images, the determinant coefficient of the random forest model was 0.4971, and it was smaller than that of the multiple linear regression model of 0.5409. However, the RMSE, MAE and rRMSE were larger than those of the multiple linear regression. For Landsat-8 images, the modeling accuracy was the worst compared with the other two satellite data AGB models, and the R^2, RMSE, MAE and rRMSE of the random forest model were 0.4235, 28.6546, 25.2203 and 0.2759, respectively. The multiple linear regression model showed worse accuracy, with R^2, RMSE, MAE and rRMSE of 0.3034, 28.8477, 23.7357 and 0.2778, respectively. Comparing the AGB modeling accuracy obtained with different modeling methods, it can be seen that the random forest model had better accuracy than the multiple linear regression model. Comparing the AGB modeling accuracy obtained with different remote sensing data, the performance of the random forest AGB model using GF-2 was the best, and it displayed a better estimation effect for the aboveground forest biomass in the research area.

To test the prediction efficiency of the model for independent samples, 25% of the sample data were used to preformed the AGB estimation. Then, the estimation accuracy was calculated, and the results can be found in Table 4.

Table 4. The comparison of the AGB prediction accuracy with various remote sensing data.

Image	Resolution	Model	R^2	RMSE	MAE	rRMSE
GF-2	4 m	Multiple Linear	0.4072	20.2781	16.9451	0.1759
		Random Forest	0.5711	16.9586	12.7153	0.1471
Sentinel-2	10 m	Multiple Linear	0.3344	23.6606	19.7257	0.2353
		Random Forest	0.4819	19.4657	14.3562	0.1936
Landsat-8	30 m	Multiple Linear	0.2892	32.8565	25.6158	0.3034
		Random Forest	0.4321	29.7677	28.0137	0.2749

The determinant coefficient between measured and estimated AGB using the random forest model with GF-2 was 0.5711, RMSE was 16.9586, MAE was 12.7153, and rRMSE was 0.1471. The R^2 when using the multi-linear regression model was 0.4072, the RMSE was 20.2781, MAE was 16.9451, and rRMSE was 0.1759. These values for Sentinel-2 using the random forest modeling method were 0.4819, 19.4657, 14.3562 and 0.1936, respectively. The multi-linear regression model results for Sentinel-2 were 0.3344, 23.6606, 19.7257 and 0.2353, respectively. The results of the random forest model for Landsat-8 were 0.4321, 29.7677, 28.0137 and 0.2749, respectively. The results of the multi-linear regression model for Landsat-8 were 0.2892, 32.8565, 25.6158 and 0.3034, respectively. It can be seen that the prediction accuracy of the random forest regression model was better than that of the multi-linear regression model.

A scatter plot of the measured and estimated AGB is shown in Figure 4. Compared with the AGB estimated by using the multi-linear regression model, AGB estimation by using the random forest model was distributed at nearly $y = x$, which indicates that the estimated AGB deviated less from the measured value, and it could perform with higher accuracy. The estimated AGB obtained using the multi-linear regression model showed a larger bias from the line of $y = x$. This meant that the model would produce a larger estimation error.

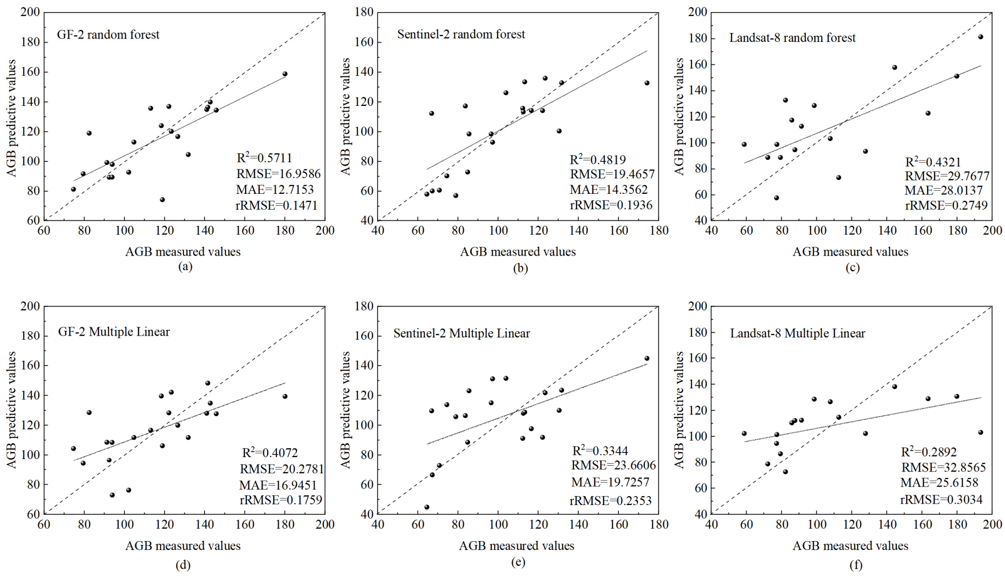

Figure 4. Scatter plot between measured and estimated AGB (black dotted line indicates $y = x$). (**a**) the scattering plot of measured and estimated AGB of GF-2 by using random forest model; (**b**) the scattering plot of measured and estimated AGB of Sentinel-2 by using random forest model; (**c**) the scattering plot of measured and estimated AGB of Landsat-8 by using random forest model; (**d**) the scattering plot of measured and estimated AGB of GF-2 by using multiple linear model; (**e**) the scattering plot of measured and estimated AGB of Sentinel-2 by using multiple linear model; (**f**) the scattering plot of measured and estimated AGB of Landsat-8 by using multiple linear model.

4.2. Retriveved AGB at Various Spatial Resolutions

First, the AGB prediction using the random forest model was performed for GF-2, Sentinel-2 and Landsat-8 images, and the AGB inversion results of GF-2 with 4 m spatial resolution ($AGB_{GF\text{-}2}$), Sentinel-2 with 10 m spatial resolution ($AGB_{Sentinel\text{-}2}$) and Landsat-8 with 30 m spatial resolution ($AGB_{Landsat\text{-}8}$) were obtained (Figure 5).

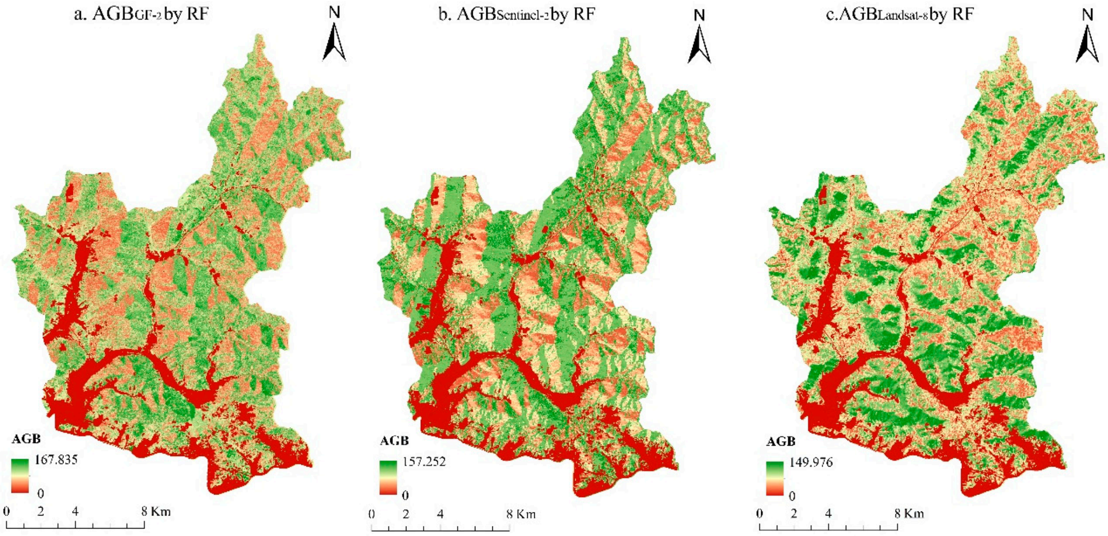

Figure 5. AGB estimation using the random forest model for various remote sensing data: (**a**) AGB estimation result using GF-2; (**b**) AGB estimation result using Sentinel-2; (**c**) AGB estimation result using Landsat-8. (Unit was t/ha).

The statistical information is summarized in Table 5. The mean of the AGB estimation of GF-2 ($AGB_{GF\text{-}2}$) was 101.30 t/ha. The standard deviation was 40.25 t/ha. The mean of the AGB estimation of Sentinel-2 ($AGB_{Sentinel\text{-}2}$) was 102.52 t/ha, with the standard deviation of 43.95 t/ha. The mean of the AGB estimation of Landsat-8 ($AGB_{Landsat\text{-}8}$) was 94.70 t/ha, with the standard deviation of 40.02 t/ha. The mean AGB estimation among GF-2 and Sentinel-2 had a similar value, but the standard deviation showed a significant difference. This meant that the AGB estimated with Sentinel-2 had a large deviation. Moreover, the mean of the AGB estimated by Landsat-8 had a significant difference compared with other two results. The differences among AGB estimation were mainly caused by the estimation error and scale effect.

Table 5. The statistical information of AGB estimation results using various remote sensing data.

Index	$\mathbf{AGB_{GF\text{-}2}}$	$\mathbf{AGB_{Sentinel\text{-}2}}$	$\mathbf{AGB_{Landsat\text{-}8}}$
Mean	101.30	102.52	94.70
Standard deviation	40.25	43.95	40.02

Then, the relative true values of AGB at 10 m ($AGB_{exa\text{-}10}$) and 30 m ($AGB_{exa\text{-}30}$) spatial resolution were calculated based on the AGB estimation using GF-2, and the AGB distribution can be found in Figure 6. The statistical information is shown in Table 6. The results show that the relative true values of AGB among the various spatial resolutions were similar, without a significant difference, and this result was consistent with our assumption. However, the relative true value of the AGB estimation had a significant bias compared with the AGB estimated using remote sensing data. The mean of the AGB estimation of Landsat-8 ($AGB_{Landsat\text{-}8}$) was 94.70 t/ha, with the standard deviation of 40.02 t/ha. The mean of the relative true value of AGB ($AGB_{exa\text{-}30}$) at the same spatial resolution was 101.24 t/ha, with the standard deviation of 37.98 t/ha. This bias of the mean value of AGB estimation was obvious. This difference can be considered as the effect of the scale error on the AGB estimation. Compared with high-spatial-resolution GF-2 data, the surface spatial heterogeneity and mixed pixels would have a greater effect on one pixel of Landsat-8. Moreover, there may be more pixels with a single property in one pixel of GF-2. This scale effect led to errors in the estimation results for different spatial resolutions.

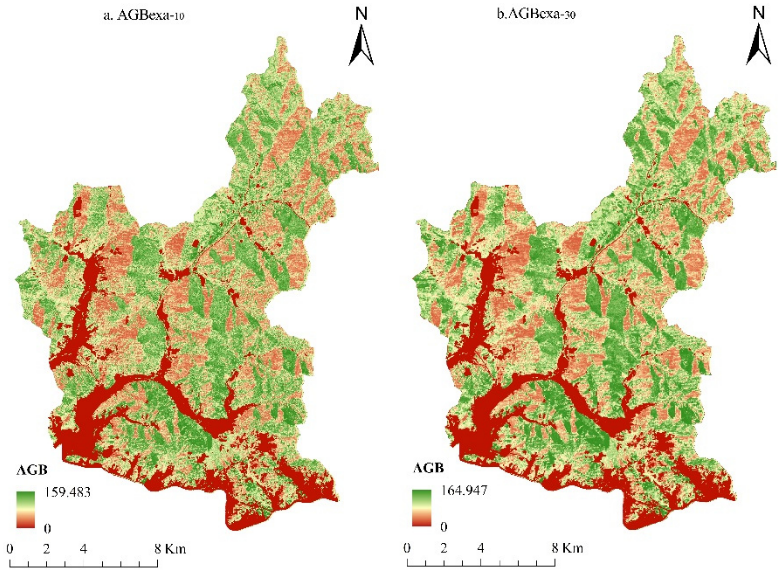

Figure 6. Relative values of the AGB extracted by using estimated AGB of GF-2 at 10 m and 30 m spatial resolution. (**a**) Relative value of the AGB of 10 m; (**b**) Relative value of the AGB of 30 m. (Unit was t/ha).

Table 6. The statistical information of relative true value of the AGB using various remote sensing data.

Index	$AGB_{GF\text{-}2}$	$AGB_{exa\text{-}10}$	$AGB_{exa\text{-}30}$
Mean	101.30	101.29	101.24
Standard deviation	40.25	39.31	37.98

4.3. Verification of the Scale Error Correction

To correct the scale error of the upscaling-based AGB estimation, a scale conversion method using the entropy-weighted index was developed based on the different land use types in one pixel of the 10 m and 30 m spatial resolution remote sensing. The $AGB_{cor\text{-}10}$ and $AGB_{cor\text{-}30}$ after scale effect correction were calculated. Comparing the relative true values of AGB at 10 m ($AGB_{exa\text{-}10}$) and 30 m ($AGB_{exa\text{-}30}$) calculated by GF-2 with the pre- and post-scale effect correction results of AGB estimation by the random forest model of Sentinel-2 and Landsat-8, the accuracy was calculated (Table 7).

Table 7. Accuracy of the scale error corrected AGB at various spatial resolutions.

Index	$AGB_{Sentinel\text{-}2}$	$AGB_{exa\text{-}10}$	$AGB_{Landsat\text{-}8}$	$AGB_{exa\text{-}30}$
MBE	11.4635	1.2378	6.0725	−6.0069
RMSE	16.3102	10.7745	9.0367	8.2139
MAPE	12.0822	7.4743	7.0241	6.3071
R^2	0.6226	0.6725	0.5910	0.6704

Comparing the relative true values of AGB with the pre- and post-correction results of AGB estimation, the MBE of the 10 m resolution corrected AGB decreased from 11.4635 to 1.2348 t/ha. The root mean squared error index of the corrected AGB of 10 m resolution had a significant improvement; the RMSE of the 10 m resolution corrected AGB decreased from 16.3102 to 10.7745 t/ha. MAPE decreased from 12.0822 to 7.4743 t/ha, and the R^2 was increased from 0.6226 to 0.6725. The scatter plots of the pre- and post-correction results are shown in Figure 7. After the scale error correction, the AGB showed a better linear relationship with the relative true value. This indicated that the scale conversion method using the entropy-weighted index had a good effect on scale error correction.

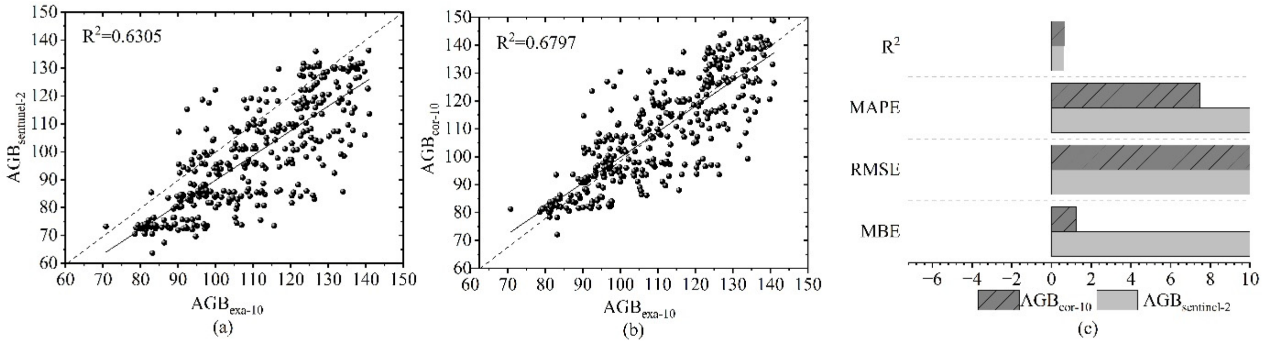

Figure 7. Scatter plot of the pre- and post-correction results and true AGB and the accuracy comparison of 10 m. (**a**) Scatter plot of the pre-correction results and true AGB at 10 m; (**b**) scatter plot of the post-correction results and true AGB at 10 m; (**c**) accuracy comparison.

Similar results were obtained for Landsat-8 AGB estimation. Comparing the relative true values of AGB with the pre- and post-correction results of Landsat-8 AGB estimation, the MBE of the 30 m resolution corrected AGB decreased from 6.0725 to −6.0069 t/ha. The RMSE decreased from 9.0367 to 8.2139 t/ha. MAPE decreased from 7.0241 to 6.3071 t/ha, and the R^2 was increased from 0.5910 to 0.6704. The scatter plots of the pre- and post-correction results of Landsat-8 AGB estimation are shown in Figure 8. There was a significant underestimation of the AGB from Landsat-8 data using the random forest model (Figure 8a). However, the scale error-corrected results were evenly distributed along the line of $y = x$, as seen in Figure 8b. This indicated that the underestimation was improved well by using the scale error correction method. The results also showed that this method can be used to correct the scale effect resulting from the heterogeneity of land use types caused by the various spatial resolutions.

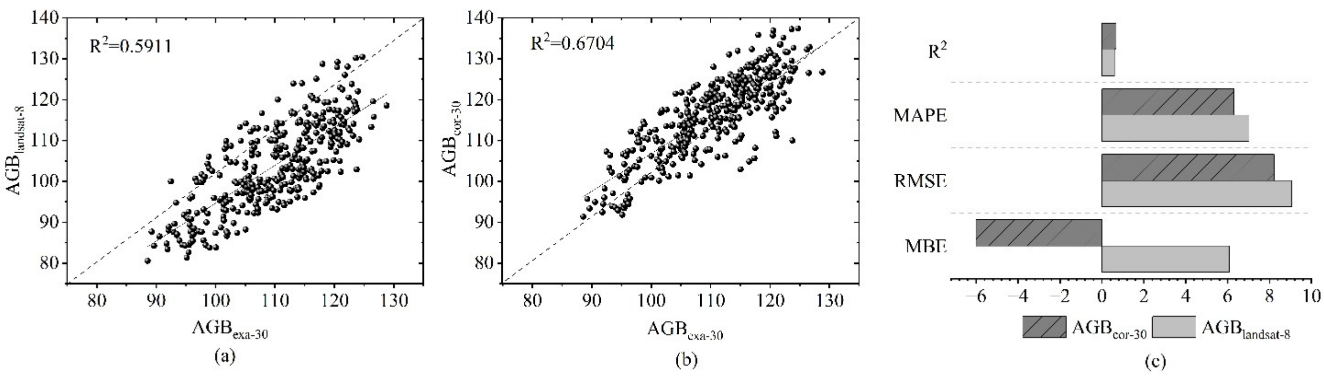

Figure 8. Scatter plot of the pre- and post-correction results and true AGB and the accuracy comparison of 30 m. (**a**) Scatter plot of the pre-correction results and true AGB at 30 m; (**b**) scatter plot of the post-correction results and true AGB at 30 m; (**c**) accuracy comparison.

Then, this scale error correction method was applied to the overall range of the study area, and the distribution of the AGB estimation based on remote sensing at the various coarse resolutions was obtained (Figure 9).

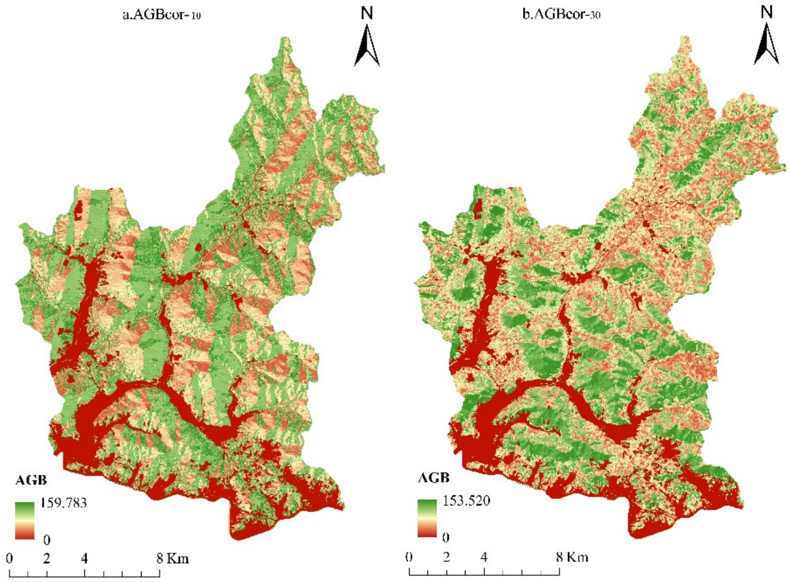

Figure 9. The scale error-corrected AGB distribution at 10 m and 30 m spatial resolution. (**a**) Corrected AGB at 10 m; (**b**) corrected AGB at 30 m. (Unit was t/ha).

5. Discussion

Forest biomass is critically important for forest dynamics in the carbon cycle [79]. However, it remains uncertain because large-scale AGB mapping applications from remote sensing data still carry large uncertainty [37,80]. In this study, a random forest model was devised to estimate the AGB at three different spatial scales (4 m, 10 m, 30 m). The determination coefficient between estimated and measured AGB for various remote sensing data using an independent dataset was 0.5711, 0.4819 and 0.4321, respectively. The same model and dataset were used, but the prediction accuracy of the AGB varied among different remote sensing data. The results generally demonstrated a tendency in which the accuracy of AGB estimation was decreased with the increase in the pixel size of the remote sensing data. In other words, there was a significant scale effect, which is the main problem associated with parameter estimation when using remote sensing. According to the results, this scale effect resulted in significant uncertainty in forest AGB estimation in this study [81].

Some scholars have focused on scale effect research and attempted to identify the reasons for the scale error. Chen found that this scale effect was caused by the surface heterogeneity. He noted that the nonlinearity of the retrieval algorithm and mixed pixels led to the scale effect of the inversion of land surface parameters [82]. Leeuwen et al. pointed out that spectral mixing would increase the error of the classification [83]. Therefore, we developed a scale error correction method using information entropy of the land use type and compared the corrected AGB results. The fitting R^2 of the AGB estimation after scale correction at a resolution of 10 m increased from 0.6226 to 0.6725, and the MBE, RMSE and MAPE were significantly decreased compared with the AGB results without correction. Compared with other similar research, the accuracy was increased [84,85]. The fitting R^2 of the AGB estimation at a resolution of 30 m before correction was 0.5910, and it increased to 0.6704 after correction. In contrast, Zhou concluded that the R^2 of AGB estimation only using Landsat-8 was 0.61 [86]. It was easily found that the correction of the scale effect can effectively improve the accuracy of AGB estimation, and our method presented good performance for scale error correction. Thus, it can be considered as an approach to correct the scale effect and improve the AGB estimation accuracy of coarse-resolution images.

To correct the scaling bias, scholars have developed many methods, such as statistical regression, the Taylor series expansion method, the wavelet fractal method, the fractal method and geostatistical theory [87]. The geostatistical method is commonly used for the upscaling of AGB over the feature space [88]. In this study, four geostatistical scale conversion methods, namely bilinear interpolation, the nearest neighbor method, cubic convolution and the Kriging interpolation method, were selected to upscale the AGB estimation from 4 m to 10 m and 30 m spatial resolution. Figure 10 shows the scatter plot of the relative true value and scale corrected using the geostatistical method for Sentinel-2 (Figure 10). The R^2 was 0.5981, 0.4354, 0.4445 and 0.6024. In contrast, the AGB results corrected by the Kriging interpolation method showed the best accuracy among these four methods. However, it was still inferior to our method, with R^2 of 0.6797. At the same time, the AGB estimation using the geostatistical scale was biased from the relative true value. The AGB value was overestimated when the AGB true value was small and vice versa. Moreover, the AGB bias was reduced using the method of this study.

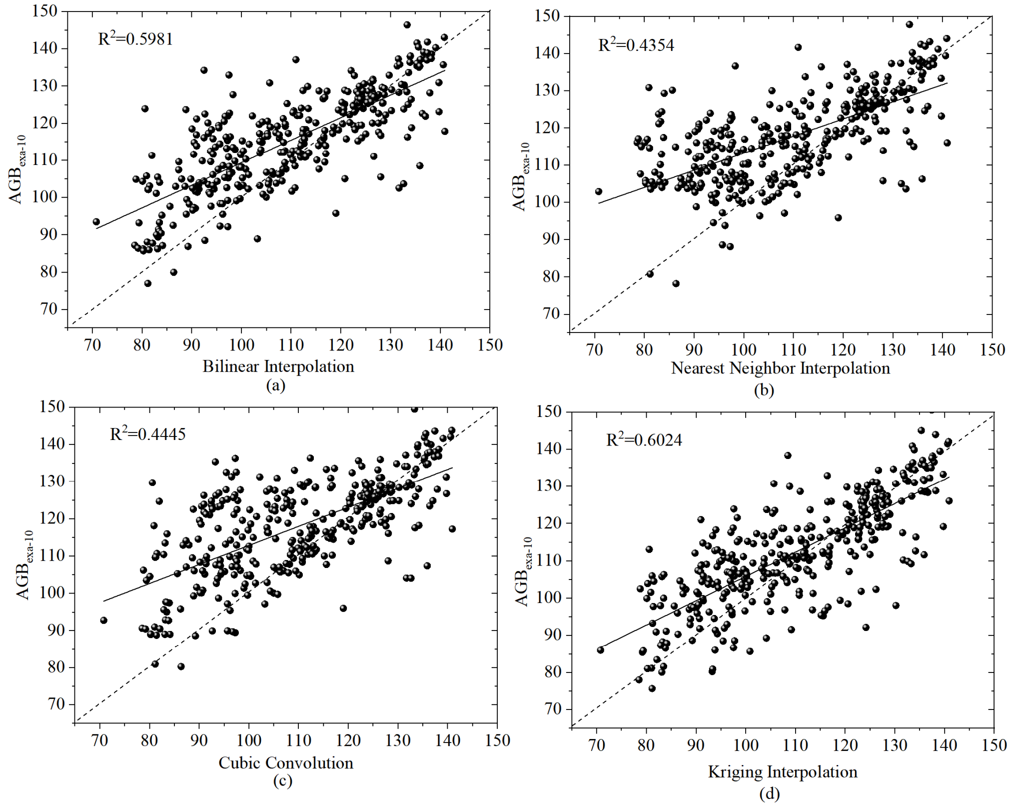

Figure 10. Scatter plot between measured and geostatistical scale-corrected AGB at 10 m resolution.

In the same way, the corrected AGB values using bilinear interpolation, the nearest neighbor method, cubic convolution and the Kriging interpolation method were also calculated and the accuracy was compared with Landsat-8 AGB estimation. The R^2 values of the four method were 0.5369, 0.4916, 0.5476 and 0.5747, respectively. Among these results, the Kriging interpolation method showed a good capacity for upscaling, with higher accuracy (Figure 11). However, the results corrected by the Kriging interpolation method still showed lower accuracy compared with the method of this study, with R^2 of 0.6704. The main reason was that a constant AGB value at different scales was selected, and it could be considered as a ruler, which was used to measure the scale error. After this, the scale conversion method with the entropy-weighted index was used to correct the scale error of the coarse-resolution image. Since the information entropy weight index considered the information entropy of the land use type, the heterogeneity of the surface feature could be fully considered. At the same time, this entropy weight index varied pixel by pixel and thus the correction index of the scale error for each pixel could be calculated, realizing the AGB scale error correction with various spatial resolutions.

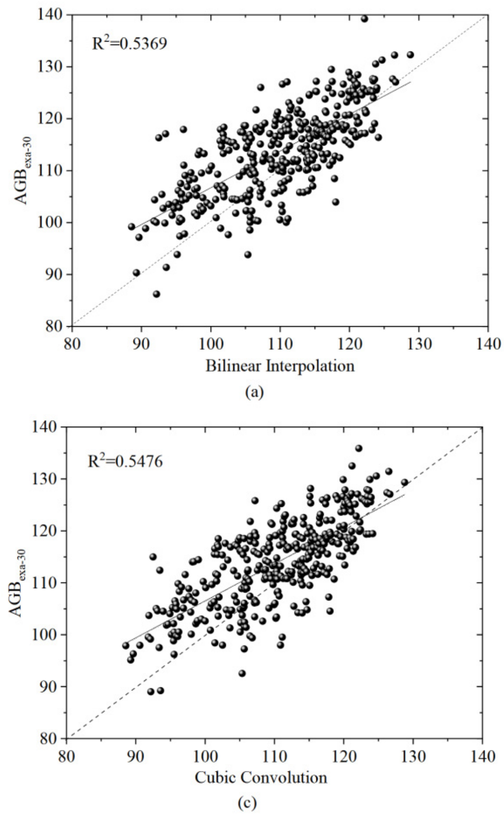

Figure 11. Accuracy evaluation among geostatistical scale-corrected AGB results at 30 m resolution.

It should be noted that some uncertainty may have existed in the current research. First, in the sample survey, there were many typical forest type survey sites selected, but the samples were still unable to cover the total research regions, so the number of the samples and the distribution of the survey sites many bring some uncertainty to the AGB estimation described in this paper. Moreover, the measurement error in the field investigation was not evaluated, and this will lead to the uncertainty of the stand aboveground biomass value calculated based on investigated data. Vegetation growth stages and seasonal differences should be considered for optical remote sensing data applications [89]. Shen et al. found that the vegetation index (VI) introduced large uncertainty in each season, and this affected the AGB estimation results [90,91]. In addition, the algorithm itself will have error transmission and introduce the uncertainty of the estimated AGB. All these issues need to be studied in further work.

6. Conclusions

In this study, a method of forest AGB modeling for three different types of remote sensing data was performed and the accuracy of AGB estimation was compared. Then, the error caused by the scale effect was analyzed and a method to correct this scale error was developed. Some valuable conclusions were as follows:

(1) The random forest model had better AGB estimation accuracy for three different spatial resolutions of remote sensing. This indicates that the nonlinear machine learning method would be promising candidate for AGB estimation.

(2) With the assumption of the law of conservation of mass, a scale error correction method using the information entropy of land use type was developed and successfully applied to the upscaling of AGB estimation for data of different resolution. Compared with other geostatistical interpolation methods, this method can obtain a high-accuracy AGB estimation and reduce the effect of the scale error on AGB estimation. The results indicated that this method can reduce the scale effect caused by the heterogeneity of the surface feature.

This research can provide a reference for AGB estimation and AGB upscaling methods at different spatial resolutions of remote sensing.

Author Contributions: Y.Y. conceived and designed the experiments; Y.P. performed the experiments and analyzed the data; X.Y. and Y.P. wrote the paper; X.Y., Y.Y. and W.F. reviewed and edited the paper. All authors have read and agreed to the published version of the manuscript.

Funding: This research was funded by the National Natural Science Foundation of China, grant numbers 31870621 and 31971580; the Fundamental Research Funds for the Central Universities of China, grant numbers 2572021BA08, 2572019BA10, and 2572019CP12; and the China Postdoctoral Science Foundation, grant number 2019M661239.

Conflicts of Interest: The authors declare no conflict of interest.

References

1. Zhang, Y.; Liang, S.; Yang, L. A review of regional and global gridded forest biomass datasets. *Remote Sens.* **2019**, *11*, 2744. [CrossRef]
2. Anderegg, W.R.; Schwalm, C.; Biondi, F.; Camarero, J.J.; Koch, G.; Litvak, M.; Ogle, K.; Shaw, J.D.; Shevliakova, E.; Williams, A. Pervasive drought legacies in forest ecosystems and their implications for carbon cycle models. *Science* **2015**, *349*, 528–532. [CrossRef] [PubMed]
3. Bonan, G.B. Forests and climate change: Forcings, feedbacks, and the climate benefits of forests. *Science* **2008**, *320*, 1444–1449. [CrossRef] [PubMed]
4. DeLucia, E.H.; Moore, D.J.; Norby, R.J. Contrasting responses of forest ecosystems to rising atmospheric CO2: Implications for the global C cycle. *Glob. Biogeochem. Cycles* **2005**, *19*, GB3006. [CrossRef]
5. Li, P.; Peng, C.; Wang, M.; Li, W.; Zhao, P.; Wang, K.; Yang, Y.; Zhu, Q. Quantification of the response of global terrestrial net primary production to multifactor global change. *Ecol. Indic.* **2017**, *76*, 245–255. [CrossRef]
6. Norby, R.J.; DeLucia, E.H.; Gielen, B.; Calfapietra, C.; Giardina, C.P.; King, J.S.; Ledford, J.; McCarthy, H.R.; Moore, D.J.; Ceulemans, R. Forest response to elevated CO_2 is conserved across a broad range of productivity. *Proc. Natl. Acad. Sci. USA* **2005**, *102*, 18052–18056. [CrossRef]
7. Canadell, J.G.; Raupach, M.R. Managing forests for climate change mitigation. *Science* **2008**, *320*, 1456–1457. [CrossRef]
8. Arora, V.K.; Melton, J.R. Reduction in global area burned and wildfire emissions since 1930s enhances carbon uptake by land. *Nat. Commun.* **2018**, *9*, 1326. [CrossRef]
9. Tang, X.; Zhao, X.; Bai, Y.; Tang, Z.; Wang, W.; Zhao, Y.; Wan, H.; Xie, Z.; Shi, X.; Wu, B. Carbon pools in China's terrestrial ecosystems: New estimates based on an intensive field survey. *Proc. Natl. Acad. Sci. USA* **2018**, *115*, 4021–4026. [CrossRef]
10. Carvalhais, N.; Forkel, M.; Khomik, M.; Bellarby, J.; Jung, M.; Migliavacca, M.; Saatchi, S.; Santoro, M.; Thurner, M.; Weber, U. Global covariation of carbon turnover times with climate in terrestrial ecosystems. *Nature* **2014**, *514*, 213–217. [CrossRef]
11. Hamilton, S.E.; Friess, D.A. Global carbon stocks and potential emissions due to mangrove deforestation from 2000 to 2012. *Nat. Clim. Chang.* **2018**, *8*, 240–244. [CrossRef]
12. Araza, A.; de Bruin, S.; Herold, M.; Quegan, S.; Labriere, N.; Rodriguez-Veiga, P.; Avitabile, V.; Santoro, M.; Mitchard, E.T.; Ryan, C.M. A comprehensive framework for assessing the accuracy and uncertainty of global above-ground biomass maps. *Remote Sens. Environ.* **2022**, *272*, 112917. [CrossRef]
13. O'Connor, B.; Bojinski, S.; Röösli, C.; Schaepman, M.E. Monitoring global changes in biodiversity and climate essential as ecological crisis intensifies. *Ecol. Inform.* **2020**, *55*, 101033. [CrossRef]
14. Rodríguez-Veiga, P.; Saatchi, S.; Tansey, K.; Balzter, H. Magnitude, spatial distribution and uncertainty of forest biomass stocks in Mexico. *Remote Sens. Environ.* **2016**, *183*, 265–281. [CrossRef]
15. Herold, M.; Carter, S.; Avitabile, V.; Espejo, A.B.; Jonckheere, I.; Lucas, R.; McRoberts, R.E.; Næsset, E.; Nightingale, J.; Petersen, R.; et al. The Role and Need for Space-Based Forest Biomass-Related Measurements in Environmental Management and Policy. *Surv. Geophys.* **2019**, *40*, 757–778. [CrossRef]
16. Hermans-Neumann, K.; Gerstner, K.; Geijzendorffer, I.R.; Herold, M.; Seppelt, R.; Wunder, S. Why do forest products become less available? A pan-tropical comparison of drivers of forest-resource degradation. *Environ. Res. Lett.* **2016**, *11*, 125010. [CrossRef]
17. Flade, L.; Hopkinson, C.; Chasmer, L. Allometric Equations for Shrub and Short-Stature Tree Aboveground Biomass within Boreal Ecosystems of Northwestern Canada. *Forests* **2020**, *11*, 1207. [CrossRef]
18. Piermattei, L.; Karel, W.; Wang, D.; Wieser, M.; Mokroš, M.; Surový, P.; Koreň, M.; Tomaštík, J.; Pfeifer, N.; Hollaus, M. Terrestrial Structure from Motion Photogrammetry for Deriving Forest Inventory Data. *Remote Sens.* **2019**, *11*, 950. [CrossRef]
19. Fang, J.; Guo, Z.; Hu, H.; Kato, T.; Muraoka, H.; Son, Y. Forest biomass carbon sinks in E ast A sia, with special reference to the relative contributions of forest expansion and forest growth. *Glob. Chang. Biol.* **2014**, *20*, 2019–2030. [CrossRef]
20. Liang, X.; Hyyppä, J.; Kaartinen, H.; Lehtomäki, M.; Pyörälä, J.; Pfeifer, N.; Holopainen, M.; Brolly, G.; Francesco, P.; Hackenberg, J.; et al. International benchmarking of terrestrial laser scanning approaches for forest inventories. *ISPRS J. Photogramm.* **2018**, *144*, 137–179. [CrossRef]

21. Mutanga, O.; Adam, E.; Cho, M.A. High density biomass estimation for wetland vegetation using WorldView-2 imagery and random forest regression algorithm. *Int. J. Appl. Earth Observ. Geoinf.* **2012**, *18*, 399–406. [CrossRef]
22. Tsitsi, B. Remote sensing of aboveground forest biomass: A review. *Trop. Ecol.* **2016**, *57*, 125–132.
23. Zhang, X.; Ni-Meister, W. Biophysical applications of satellite remote sensing. *Remote Sens. For. Biomass* **2014**, 63–98. [CrossRef]
24. Nian, V. The carbon neutrality of electricity generation from woody biomass and coal, a critical comparative evaluation. *Appl. Energy* **2016**, *179*, 1069–1080. [CrossRef]
25. Hayashi, M.; Saigusa, N.; Yamagata, Y.; Hirano, T. Regional forest biomass estimation using ICESat/GLAS spaceborne LiDAR over Borneo. *Carbon Manag.* **2015**, *6*, 19–33. [CrossRef]
26. Urbazaev, M.; Thiel, C.; Cremer, F.; Dubayah, R.; Migliavacca, M.; Reichstein, M.; Schmullius, C. Estimation of forest aboveground biomass and uncertainties by integration of field measurements, airborne LiDAR, and SAR and optical satellite data in Mexico. *Carbon Balance Manag.* **2018**, *13*, 5. [CrossRef]
27. Migolet, P.; Goïta, K.; Pambo, A.F.K.; Mambimba, A.N. Estimation of the total dry aboveground biomass in the tropical forests of Congo Basin using optical, LiDAR, and radar data. *GISci. Remote Sens.* **2022**, *59*, 431–460. [CrossRef]
28. Nguyen, T.H.; Jones, S.; Soto-Berelov, M.; Haywood, A.; Hislop, S. Landsat time-series for estimating forest aboveground biomass and its dynamics across space and time: A review. *Remote Sens.* **2019**, *12*, 98. [CrossRef]
29. Hlatshwayo, S.T.; Mutanga, O.; Lottering, R.T.; Kiala, Z.; Ismail, R. Mapping forest aboveground biomass in the reforested Buffelsdraai landfill site using texture combinations computed from SPOT-6 pan-sharpened imagery. *Int. J. Appl. Earth Observ. Geoinf.* **2019**, *74*, 65–77. [CrossRef]
30. Zhu, Y.; Liu, K.; Myint, S.W.; Du, Z.; Li, Y.; Cao, J.; Liu, L.; Wu, Z. Integration of GF2 optical, GF3 SAR, and UAV data for estimating aboveground biomass of China's largest artificially planted mangroves. *Remote Sens.* **2020**, *12*, 2039. [CrossRef]
31. Yuan, X.; Li, L.; Tian, X.; Luo, G.; Chen, X. Estimation of above-ground biomass using MODIS satellite imagery of multiple land-cover types in China. *Remote Sens. Lett.* **2016**, *7*, 1141–1149. [CrossRef]
32. Yu, R.; Yao, Y.; Wang, Q.; Wan, H.; Xie, Z.; Tang, W.; Zhang, Z.; Yang, J.; Shang, K.; Guo, X.; et al. Satellite-Derived Estimation of Grassland Aboveground Biomass in the Three-River Headwaters Region of China during 1982–2018. *Remote Sens.* **2021**, *13*, 2993. [CrossRef]
33. Lu, D.; Chen, Q.; Wang, G.; Liu, L.; Li, G.; Moran, E. A survey of remote sensing-based aboveground biomass estimation methods in forest ecosystems. *Int. J. Digit. Earth* **2016**, *9*, 63–105. [CrossRef]
34. Zhao, P.; Lu, D.; Wang, G.; Wu, C.; Huang, Y.; Yu, S. Examining spectral reflectance saturation in Landsat imagery and corresponding solutions to improve forest aboveground biomass estimation. *Remote Sens.* **2016**, *8*, 469. [CrossRef]
35. Hernández-Stefanoni, J.L.; Castillo-Santiago, M.Á.; Mas, J.F.; Wheeler, C.E.; Andres-Mauricio, J.; Tun-Dzul, F.; George-Chacón, S.P.; Reyes-Palomeque, G.; Castellanos-Basto, B.; Vaca, R. Improving aboveground biomass maps of tropical dry forests by integrating LiDAR, ALOS PALSAR, climate and field data. *Carbon Balance Manag.* **2020**, *15*, 1–17. [CrossRef]
36. Réjou-Méchain, M.; Tanguy, A.; Piponiot, C.; Chave, J.; Hérault, B. biomass: An R package for estimating above-ground biomass and its uncertainty in tropical forests. *Methods Ecol. Evolut.* **2017**, *8*, 1163–1167. [CrossRef]
37. Réjou-Méchain, M.; Barbier, N.; Couteron, P.; Ploton, P.; Vincent, G.; Herold, M.; Mermoz, S.; Saatchi, S.; Chave, J.; de Boissieu, F.; et al. Upscaling Forest Biomass from Field to Satellite Measurements: Sources of Errors and Ways to Reduce Them. *Surv. Geophy.* **2019**, *40*, 881–911. [CrossRef]
38. Chen, Q.; Laurin, G.V.; Valentini, R. Uncertainty of remotely sensed aboveground biomass over an African tropical forest: Propagating errors from trees to plots to pixels. *Remote Sens. Environ.* **2015**, *160*, 134–143. [CrossRef]
39. Longo, M.; Keller, M.; dos-Santos, M.N.; Leitold, V.; Pinage, E.R.; Baccini, A.; Saatchi, S.; Nogueira, E.M.; Batistella, M.; Morton, D.C. Aboveground biomass variability across intact and degraded forests in the Brazilian Amazon. *Glob. Biogeochem. Cycles* **2016**, *30*, 1639–1660. [CrossRef]
40. Mascaro, J.; Detto, M.; Asner, G.P.; Muller-Landau, H.C. Evaluating uncertainty in mapping forest carbon with airborne LiDAR. *Remote Sens. Environ.* **2011**, *115*, 3770–3774. [CrossRef]
41. Avitabile, V.; Camia, A. An assessment of forest biomass maps in Europe using harmonized national statistics and inventory plots. *For. Ecol. Manag.* **2018**, *409*, 489–498. [CrossRef] [PubMed]
42. Næsset, E.; Bollandsås, O.M.; Gobakken, T.; Solberg, S.; McRoberts, R.E. The effects of field plot size on model-assisted estimation of aboveground biomass change using multitemporal interferometric SAR and airborne laser scanning data. *Remote Sens. Environ.* **2015**, *168*, 252–264. [CrossRef]
43. Persson, H.J.; Ståhl, G. Characterizing Uncertainty in Forest Remote Sensing Studies. *Remote Sens.* **2020**, *12*, 505. [CrossRef]
44. Chambers, J.Q.; Negron-Juarez, R.I.; Marra, D.M.; Di Vittorio, A.; Tews, J.; Roberts, D.; Ribeiro, G.H.; Trumbore, S.E.; Higuchi, N. The steady-state mosaic of disturbance and succession across an old-growth Central Amazon forest landscape. *Proc. Natl. Acad. Sci. USA* **2013**, *110*, 3949–3954. [CrossRef]
45. Shen, X.; Jiang, M.; Lu, X.; Liu, X.; Liu, B.; Zhang, J.; Wang, X.; Tong, S.; Lei, G.; Wang, S. Aboveground biomass and its spatial distribution pattern of herbaceous marsh vegetation in China. *Sci. China Earth Sci.* **2021**, *64*, 1115–1125. [CrossRef]
46. Rejou-Mechain, M.; Muller-Landau, H.C.; Detto, M.; Thomas, S.C.; Le Toan, T.; Saatchi, S.S.; Barreto-Silva, J.S.; Bourg, N.A.; Bunyavejchewin, S.; Butt, N. Local spatial structure of forest biomass and its consequences for remote sensing of carbon stocks. *Biogeosciences* **2014**, *11*, 6827–6840. [CrossRef]

47. Masinda, M.M.; Li, F.; Liu, Q.; Sun, L.; Hu, T. Prediction model of moisture content of dead fine fuel in forest plantations on Maoer Mountain, Northeast China. *J. For. Res.* **2021**, *32*, 2023–2035. [CrossRef]
48. Wang, C. Biomass allometric equations for 10 co-occurring tree species in Chinese temperate forests. *For. Ecol. Manag.* **2006**, *222*, 9–16. [CrossRef]
49. Zheng, Y.; Dai, Q.; Tu, Z.; Wang, L. Guided Image Filtering-Based Pan-Sharpening Method: A Case Study of GaoFen-2 Imagery. *ISPRS Int. J. Geo-Inf.* **2017**, *6*, 404. [CrossRef]
50. Kobayashi, N.; Tani, H.; Wang, X.; Sonobe, R. Crop classification using spectral indices derived from Sentinel-2A imagery. *J. Inf. Telecommun.* **2020**, *4*, 67–90. [CrossRef]
51. López-Serrano, P.M.; Cardenas Dominguez, J.L.; Corral-Rivas, J.J.; Jiménez, E.; López-Sánchez, C.A.; Vega-Nieva, D.J. Modeling of aboveground biomass with Landsat 8 OLI and machine learning in temperate forests. *Forests* **2019**, *11*, 11. [CrossRef]
52. Dong, L.; Zhang, L.; Li, F. A compatible system of biomass equations for three conifer species in Northeast, China. *For. Ecol. Manag.* **2014**, *329*, 306–317. [CrossRef]
53. Xu, L.; Shi, Y.; Fang, H.; Zhou, G.; Xu, X.; Zhou, Y.; Tao, J.; Ji, B.; Xu, J.; Li, C. Vegetation carbon stocks driven by canopy density and forest age in subtropical forest ecosystems. *Sci. Total Environ.* **2018**, *631*, 619–626. [CrossRef] [PubMed]
54. Taddese, H.; Asrat, Z.; Burud, I.; Gobakken, T.; Ørka, H.O.; Dick, Ø.B.; Næsset, E. Use of Remotely Sensed Data to Enhance Estimation of Aboveground Biomass for the Dry Afromontane Forest in South-Central Ethiopia. *Remote Sens.* **2020**, *12*, 3335. [CrossRef]
55. Wang, F.; Yang, M.; Ma, L.; Zhang, T.; Qin, W.; Li, W.; Zhang, Y.; Sun, Z.; Wang, Z.; Li, F.; et al. Estimation of Above-Ground Biomass of Winter Wheat Based on Consumer-Grade Multi-Spectral UAV. *Remote Sens.* **2022**, *14*, 1251. [CrossRef]
56. Ding, Z.; Sun, Y.; Sun, Z. Estimation of tree biomass with GF-2. *J. Beijing Norm. Univ.* **2021**, *57*, 135–141. [CrossRef]
57. Chen, L.; Wang, Y.; Ren, C.; Zhang, B.; Wang, Z. Assessment of multi-wavelength SAR and multispectral instrument data for forest aboveground biomass mapping using random forest kriging. *For. Ecol. Manag.* **2019**, *447*, 12–25. [CrossRef]
58. Shao, Z.; Zhang, L.; Wang, L. Stacked Sparse Autoencoder Modeling Using the Synergy of Airborne LiDAR and Satellite Optical and SAR Data to Map Forest Above-Ground Biomass. *IEEE J-Stars* **2017**, *10*, 5569–5582. [CrossRef]
59. Shi, T.; Xu, H. Derivation of Tasseled Cap Transformation Coefficients for Sentinel-2 MSI At-Sensor Reflectance Data. *IEEE J-Stars* **2019**, *12*, 4038–4048. [CrossRef]
60. Xu, T.; Cao, L.; Shen, X.; She, G. Estimates of subtropical forest biomass based on airborne LiDAR and Landsat 8 OLI data. *Chin. J. Plant Ecol.* **2015**, *39*, 309–321. [CrossRef]
61. Breiman, L. Random forests. *MLear* **2001**, *45*, 5–32. [CrossRef]
62. Zeng, N.; Ren, X.; He, H.; Zhang, L.; Zhao, D.; Ge, R.; Li, P.; Niu, Z. Estimating grassland aboveground biomass on the Tibetan Plateau using a random forest algorithm. *Ecol. Indic.* **2019**, *102*, 479–487. [CrossRef]
63. Vargas-Larreta, B.; López-Martínez, J.O.; González, E.J.; Corral-Rivas, J.J.; Hernández, F.J. Assessing above-ground biomass-functional diversity relationships in temperate forests in northern Mexico. *For. Ecosyst.* **2021**, *8*, 8. [CrossRef]
64. Ferraz, A.; Saatchi, S.; Mallet, C.; Jacquemoud, S.; Gonçalves, G.; Silva, C.A.; Soares, P.; Tomé, M.; Pereira, L. Airborne Lidar Estimation of Aboveground Forest Biomass in the Absence of Field Inventory. *Remote Sens.* **2016**, *8*, 653. [CrossRef]
65. Liu, L. Simulation and correction of spatialscaling effects for leaf area index. *J. Remote Sens.* **2014**, *18*, 1158–1168. [CrossRef]
66. Hu, X.; Xu, H. A new remote sensing index for assessing the spatial heterogeneity in urban ecological quality: A case from Fuzhou City, China. *Ecol. Indic.* **2018**, *89*, 11–21. [CrossRef]
67. Gelybó, G.; Barcza, Z.; Kern, A.; Kljun, N. Effect of spatial heterogeneity on the validation of remote sensing based GPP estimations. *Agr. For. Meteorol.* **2013**, *174*, 43–53. [CrossRef]
68. Wu, L.; Liu, X.-N.; Zheng, X.; Qin, Q.-M.; Ren, H.-Z.; Sun, Y.-J. Spatial scaling transformation modeling based on fractal theory for the leaf area index retrieved from remote sensing imagery. *J. Appl. Remote Sens.* **2015**, *9*, 096015. [CrossRef]
69. Garrigues, S.; Allard, D.; Baret, F.; Weiss, M. Influence of landscape spatial heterogeneity on the non-linear estimation of leaf area index from moderate spatial resolution remote sensing data. *Remote Sens. Environ.* **2006**, *105*, 286–298. [CrossRef]
70. Whelen, T.; Siqueira, P. Coefficient of variation for use in crop area classification across multiple climates. *Int. J. Appl. Earth Observ. Geoinf.* **2018**, *67*, 114–122. [CrossRef]
71. Li, G.; Zhao, Y.; Zhang, L.; Wang, X.; Zhang, Y.; Guo, F. Entropy-based global and local weight adaptive image segmentation models. *Tsinghua Sci. Technol.* **2019**, *25*, 149–160. [CrossRef]
72. Yang, X.; He, P.; Yu, Y.; Fan, W. Stand Canopy Closure Estimation in Planted Forests Using a Geometric-Optical Model Based on Remote Sensing. *Remote Sens.* **2022**, *14*, 1983. [CrossRef]
73. Wang, D.; Wan, B.; Liu, J.; Su, Y.; Guo, Q.; Qiu, P.; Wu, X. Estimating aboveground biomass of the mangrove forests on northeast Hainan Island in China using an upscaling method from field plots, UAV-LiDAR data and Sentinel-2 imagery. *Int. J. Appl. Earth Observ. Geoinf.* **2020**, *85*, 101986. [CrossRef]
74. Zhang, R.; Zhou, X.; Ouyang, Z.; Avitabile, V.; Qi, J.; Chen, J.; Giannico, V. Estimating aboveground biomass in subtropical forests of China by integrating multisource remote sensing and ground data. *Remote Sens. Environ.* **2019**, *232*, 111341. [CrossRef]
75. Li, C.; Li, Y.; Li, M. Improving Forest Aboveground Biomass (AGB) Estimation by Incorporating Crown Density and Using Landsat 8 OLI Images of a Subtropical Forest in Western Hunan in Central China. *Forests* **2019**, *10*, 104. [CrossRef]
76. López-Serrano, P.M.; López-Sánchez, C.A.; Álvarez-González, J.G.; García-Gutiérrez, J. A Comparison of Machine Learning Techniques Applied to Landsat-5 TM Spectral Data for Biomass Estimation. *Can. J. Remote Sens.* **2016**, *42*, 690–705. [CrossRef]

77. Zhang, L.; Shao, Z.; Liu, J.; Cheng, Q. Deep learning based retrieval of forest aboveground biomass from combined LiDAR and landsat 8 data. *Remote Sens.* **2019**, *11*, 1459. [CrossRef]
78. Dong, L.; Du, H.; Han, N.; Li, X.; Zhu, D.E.; Mao, F.; Zhang, M.; Zheng, J.; Liu, H.; Huang, Z. Application of convolutional neural network on Lei Bamboo above-ground-biomass (AGB) estimation using Worldview-2. *Remote Sens.* **2020**, *12*, 958. [CrossRef]
79. Gora, E.M.; Esquivel-Muelbert, A. Implications of size-dependent tree mortality for tropical forest carbon dynamics. *Nat. Plants* **2021**, *7*, 384–391. [CrossRef]
80. Rodríguez-Veiga, P.; Wheeler, J.; Louis, V.; Tansey, K.; Balzter, H. Quantifying forest biomass carbon stocks from space. *Curr. For. Rep.* **2017**, *3*, 1–18. [CrossRef]
81. Pearson, T.R.H.; Brown, S.; Murray, L.; Sidman, G. Greenhouse gas emissions from tropical forest degradation: An underestimated source. *Carbon Balance Manag.* **2017**, *12*, 3. [CrossRef] [PubMed]
82. Chen, J.M. Spatial Scaling of a Remotely Sensed Surface Parameter by Contexture. *Remote Sens. Environ.* **1999**, *69*, 30–42. [CrossRef]
83. van Leeuwen, M.; Frye, H.A.; Wilson, A.M. Understanding limits of species identification using simulated imaging spectroscopy. *Remote Sens. Environ.* **2021**, *259*, 112405. [CrossRef]
84. Chen, Y.; Li, L.; Lu, D.; Li, D. Exploring bamboo forest aboveground biomass estimation using Sentinel-2 data. *Remote Sens.* **2018**, *11*, 7. [CrossRef]
85. Puliti, S.; Hauglin, M.; Breidenbach, J.; Montesano, P.; Neigh, C.S.R.; Rahlf, J.; Solberg, S.; Klingenberg, T.F.; Astrup, R. Modelling above-ground biomass stock over Norway using national forest inventory data with ArcticDEM and Sentinel-2 data. *Remote Sens. Environ.* **2020**, *236*, 111501. [CrossRef]
86. Li, Y.; Li, M.; Li, C.; Liu, Z. Forest aboveground biomass estimation using Landsat 8 and Sentinel-1A data with machine learning algorithms. *Sci. Rep.* **2020**, *10*, 9952. [CrossRef]
87. Jiang, J.; Ji, X.; Yao, X.; Tian, Y.; Zhu, Y.; Cao, W.; Cheng, T. Evaluation of Three Techniques for Correcting the Spatial Scaling Bias of Leaf Area Index. *Remote Sens.* **2018**, *10*, 221. [CrossRef]
88. Propastin, P. Large-scale mapping of aboveground biomass of tropical rainforest in Sulawesi, Indonesia, using Landsat ETM+ and MODIS data. *GISci. Remote Sens.* **2013**, *50*, 633–651. [CrossRef]
89. Wang, Q.; Li, J.; Jin, T.; Chang, X.; Zhu, Y.; Li, Y.; Sun, J.; Li, D. Comparative analysis of Landsat-8, Sentinel-2, and GF-1 data for retrieving soil moisture over wheat farmlands. *Remote Sens.* **2020**, *12*, 2708. [CrossRef]
90. Wang, Z.; Wang, H.; Wang, T.; Wang, L.; Liu, X.; Zheng, K.; Huang, X. Large discrepancies of global greening: Indication of multi-source remote sensing data. *Glob. Ecol. Conserv.* **2022**, *34*, e02016. [CrossRef]
91. Shen, X.; Liu, B.; Henderson, M.; Wang, L.; Jiang, M.; Lu, X. Vegetation greening, extended growing seasons, and temperature feedbacks in warming temperate grasslands of China. *J. Clim.* **2022**, 1–51. [CrossRef]